

# In Situ Atomic Force Microscopy Study of the Dissolution Kinetics of Dicalcium Phosphate Dihydrate Crystal in a Physiological Solution

Kazuo Onuma,<sup>\*,†,‡</sup> Atsuo Ito,<sup>†</sup> Ikuko Tabe,<sup>†</sup> and Tetsuya Tateishi<sup>†</sup>

National Institute for Advanced Interdisciplinary Research, 1-1-4 Higashi, Tsukuba, Ibaraki, 305 Japan, and National Institute of Materials and Chemical Research, 1-1 Higashi, Tsukuba, Ibaraki, 305 Japan

Received: June 6, 1997; In Final Form: August 8, 1997<sup>⊗</sup>

The dissolution kinetics of the (010) face of dicalcium phosphate dihydrate crystals in a physiological solution were investigated by *in situ* atomic force microscopy. Although many etch pits with 0.75 nm high elementary steps were formed, spiral dissolution was hardly ever observed. Step velocity showed strong dependence on the crystallographic orientation and decreased with decrease of the interstep distance. From the ratio of the step kinetic coefficient to the characteristic diffusion rate, it was concluded that the dissolution process under the present conditions was controlled by detachment of molecules at a step front and surface diffusion.

## Introduction

The recent development of atomic force microscopy (AFM) has enabled real time observation and measurement of growth and dissolution processes of crystals in solution with extremely high resolution.<sup>1–4</sup> This has greatly contributed to the direct comparison of the crystal growth theory with the experiments on an atomic level. Calcium phosphate minerals are suitable samples for AFM observation because their slow growth and dissolution kinetics have rendered clarification of their mechanism by normal optical microscopy impossible.<sup>5</sup> Growth and dissolution of dicalcium phosphate dihydrate (DCPD) crystals,  $\text{CaHPO}_4 \cdot 2\text{H}_2\text{O}$ , play an important role in vertebrate biological mineralization process as well as the setting of a variety of calcium phosphate cements for orthopedic and dental use.<sup>6–8</sup> DCPD is thought to be one of the precursors of hydroxyapatite (HAP), the major component of human bone and teeth, although this idea remains to be confirmed.<sup>9–13</sup> It was, however, confirmed *in vitro* that nucleated DCPD gradually transforms to HAP crystals under physiological conditions, at neutral pH.<sup>9,10</sup> The solvent-mediated transformation process, which involves dissolution of DCPD followed by precipitation of HAP, is one of the leading models of the transformation mechanism. Thus, the dissolution kinetics of DCPD has been of much interest to many scientists. Representative studies were made by Nancollas and Marshall<sup>14</sup> and by Christoffersen and Christoffersen.<sup>15,16</sup> These two groups measured the dissolution rate of bulk crystals and investigated the dissolution mechanism from the viewpoint of the rate-determining process of dissolution. Nancollas and Marshall concluded that diffusion controls the entire dissolution process, on the basis of an estimation of the activation energy of diffusion. In contrast, Christoffersen and Christoffersen proposed the importance of kink nucleation at steps as the rate-determining process. Zhang and Nancollas showed the role of combined volume and surface diffusion processes in 1987.<sup>17</sup> They also investigated the validity of previous studies using rate equations of crystal growth<sup>18–21</sup> and concluded that volume diffusion plays an important role at high undersaturations and under mild agitation conditions of the solution, whereas the

surface process becomes important at low undersaturations.<sup>22</sup> The importance of kink formation at steps was negated. The surface process involves detachment of molecules at the step front and surface diffusion. It seems that Zhang and Nancollas were the ones who realized the importance of surface diffusion. Their studies are well documented and serve as an important guide to the dissolution kinetics of DCPD; however, to arrive at a definitive conclusion, direct measurements are necessary because all of the previous discussions were based on the results of indirect measurements. *In situ* observation of the dissolution process and direct measurement of step velocity gives us the most reliable and conclusive information on the dissolution mechanism of DCPD. The aim of this study is, therefore, to clarify the dissolution mechanism of DCPD by *in situ* AFM. We selected pseudo-physiological conditions for dissolution experiments, taking into account the importance of DCPD *in vivo*. Special attention is given to the rate-determining process of dissolution from measurements of step kinetics.

## Experimental Section

**1. Synthesis of DCPD Single Crystals.** DCPD crystals were synthesized by a wet process as follows. Calcium acetate,  $(\text{CH}_3\text{COO})_2\text{Ca}$ , and sodium dihydrogen phosphate,  $\text{NaH}_2\text{PO}_4$ , solutions, both of which were 0.04 M in concentration, were prepared. The  $(\text{CH}_3\text{COO})_2\text{Ca}$  solution was prepared from acetic acid (Wako Chemical Co., Ltd.) and ultrapure calcium carbonate powder (Calceed Co., Ltd.). Both reagents were dissolved in ultrapure sterile water to the desired concentration. The  $\text{NaH}_2\text{PO}_4$  solution was prepared by dissolving sodium dihydrogen phosphate (Hani Kagaku Co., Ltd.) in ultrapure sterile water. These procedures were performed in air at room temperature.  $\text{N}_2$  gas was bubbled into the solutions for about 20 min to remove  $\text{CO}_2$ , and the pH was adjusted to about 5.5 using 1 N sodium hydroxide solution or acetic acid solution. 100 mL of the  $\text{NaH}_2\text{PO}_4$  solution was stirred in a three-neck round-bottomed flask placed in a water bath maintained at 62 °C, and dropwise titration at a rate of 1 drop/4 with 130 mL of the  $(\text{CH}_3\text{COO})_2\text{Ca}$  solution was performed in a  $\text{N}_2$  atmosphere. Precipitation was observed about 2 h after the start of titration. The precipitate was filtered through a filter of 0.22  $\mu\text{m}$  pore size, washed with ultrapure sterile water, and air-dried. Most of the precipitates are platelike crystals from 0.5 to 1.5 mm in size. Characterization of the precipitate was performed by X-ray powder diffraction (Rigaku Denki Co., Ltd.) with  $\text{Cu K}\alpha$  wavelength at 40 kV, 40 mA, and 2.0° scan/min.

\* To whom correspondence should be addressed. Address: National Institute for Advanced Interdisciplinary Research, Bionic Design Group, 1-1-4 Higashi, Tsukuba, Ibaraki, 305 Japan. Tel.: +81-298-54-2557. Fax: +81-298-54-2565. E-mail: onuma@nair.go.jp.

<sup>†</sup> National Institute for Advanced Interdisciplinary Research.

<sup>‡</sup> National Institute of Materials and Chemical Research.

<sup>⊗</sup> Abstract published in *Advance ACS Abstracts*, October 1, 1997.

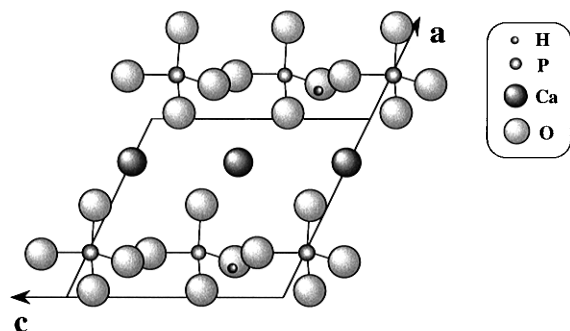


**Figure 1.** Crystal structure of DCPD viewed perpendicular to the *b* axis. Only  $\text{CaHPO}_4$  layer is seen.

**2. Solution for DCPD Dissolution.** The pseudo-physiological solution used in this study contained 140 mM NaCl, 2.5 mM  $\text{CaCl}_2$ , and 1 mM  $\text{K}_2\text{HPO}_4 \cdot 3\text{H}_2\text{O}$  buffered at pH 7.4 using tris-aminomethane and 1 N HCl. Before addition of any reagent, ultrapure sterile water, the solvent, was boiled and bubbled with  $\text{N}_2$  gas for 30 min for removal of all dissolved  $\text{CO}_2$  gas.

**3. Atomic Force Microscopy.** Observations and measurements were carried out using a NanoScope III-a AFM (Digital Instruments, Inc.) in the contact and fluid-tapping modes. The cell for the fluid-tapping mode is commercially available. Fresh solution was introduced into the cell hourly using a syringe. Oxide-sharpened silicon nitride cantilevers with a spring constant of 0.58 N/m and E-type (10  $\mu\text{m}$  scanning range) and J-type (100  $\mu\text{m}$  scanning range) piezo scanners were used for all measurements. The entire system was placed in a thermostated room and was allowed to equilibrate prior to the measurements. The dissolution temperature was fixed at 25  $^\circ\text{C}$  to avoid thermal drift of the scanner. All AFM images presented in this study were taken in the constant "height mode". For atomic-scale imaging and measurement of step velocity, contact mode observation was utilized, whereas for qualitative observation of surface features over a wide scanning range, fluid-tapping mode was used. Atomic images were analyzed by two-dimensional fast Fourier transformation.

## Results

**1. X-ray Diffraction.** An XRD pattern of the precipitate indicates that all peaks match those obtained using a DCPD standard in Joint Committee on Powder Diffraction Standards card. (The data is not shown.) The most intense peak indicates the (020) reflection of DCPD single crystals. The precipitate is therefore DCPD and its platelike morphology indicates a well-developed (010) face.

**2. Relationship between Etch Pit Orientation and Crystallographic Axis.** DCPD belongs to a monoclinic system with lattice constants  $a = 0.581$  nm,  $b = 1.518$  nm,  $c = 0.624$  nm, and  $\beta = 116^\circ 25'$ . The crystal structure of DCPD<sup>23</sup> is schematically shown in Figure 1. Figure 2a shows macroscopically the surface topography of a seed crystal observed by AFM in air. Before a DCPD single crystal was dissolved in the AFM cell, the crystal was etched with 1 N HCl for 2–3 s to remove dust adsorbed on its surface. Deeply etched rhomboidal pits as well as triangular pits appeared after this process as shown in Figure 2a. Since the irregular external form of the crystal makes it impossible to distinguish the relationship between etch pits and crystallographic orientation, atomic images obtained by AFM were utilized to determine the orientation. Figure 2b shows an 8 nm scaled atomic image taken *in situ* during crystal dissolution in the AFM cell. The raw image is shown in the lower part of the figure. When two-dimensional fast Fourier transformation

was applied to this image, four clear spots appeared as shown in the upper left corner of the figure. The upper part of this Figure shows the atomic image after fast Fourier transformation. Two periodicities with lattice constants of  $0.56 \pm 0.03$  nm and  $0.64 \pm 0.04$  nm, are clearly observed. These values correspond to the lattice constants of the *a* and *c* axes of DCPD crystals. The angle between the *a* and *c* axes in Figure 2b is  $117^\circ$ , which coincides with the value of  $\beta$  in the DCPD crystal lattice. It should be noted that the atomic images sometimes showed a pseudo-hexagonal symmetry with the lattice constant of 0.64 nm both for *a* and *c* directions, as shown in Figure 2c. This image may be an artifact because the lattice constants of the *a* and *c* axes of DCPD are similar (only 10% difference), and the  $\beta$  is very close to the angle of hexagonal symmetry,  $120^\circ$ . Scanning at a higher force seems to play some role in revealing the hexagonally symmetric atomic image; however, a clear explanation for the appearance of hexagonally symmetrical atomic images is now obscure. Arrows in Figure 2b confirm that the step orientations of rhomboidal etch pits appeared after etching at low pH correspond to [001] and [101].

**3. Appearance of Etch Pits and Steps During Dissolution in Physiological Solution.** Figure 3 shows three kinds of etch pits and steps observed during dissolution in physiological solution. Crystallographic *a* and *c* axes are superimposed in Figure 3a. Figures 3a, c are normal images, while Figures 3b, d are error signal images because the normal images have too much contrast which prevents detailed inspection. In Figures 3a, b, repeated formation of the etch pits was observed, while in Figure 3c, only one pit was formed. The center of the etch pit in Figure 3a is the front of macro steps as shown by the white arrow. In Figures 3b, c, etch pits appear on a flat terrace. The steps shown in Figure 3 are all  $0.75 \pm 0.05$  nm high and correspond to half the size of the lattice constant of the *b* axis, as seen in the cross-sectional profile in Figure 3c. The first and second kinds of etch pit are frequently formed in the dissolution process; however, the third kind of etch pit temporarily appears and cannot exist for a long time. It should be noted that the etch pits are not spiral dissolution etch pits. Indeed, spiral dissolution from dislocations with a screw component was rarely observed. All kinds of etch pits in Figure 3 are flat-bottom type suggesting that the etch pit is formed by two-dimensional nucleation, or microdefect such as point defect is the origin of the etch pits. It can be seen that the morphology of the etch pits appearing under the present conditions is completely different from the rhomboidal etch pit and resembles the triangular etch pit shown in Figure 2a. Four major step orientations except [100] and [001] were distinguished. We call these *x*-, *y*-, *z*-, and *r*-oriented steps as shown in Figure 3. The *x*- and *r*-oriented steps are inclined by  $4\text{--}5^\circ$  from [102] to [001] and [100], respectively. The *y*-oriented step is inclined by about  $4\text{--}5^\circ$  from [10 $\bar{2}$ ] to [00 $\bar{1}$ ], and the *z*-oriented step, by  $4\text{--}5^\circ$  from [201] to [100]. In addition to these steps, steps running parallel to [101] are observed. These five kinds of steps were used for the measurement of step velocities.

Etch pit morphology changes with dissolution due to the marked difference in step velocities, which is dependent on orientation. The *r*-oriented steps sometimes disappear. Anisotropic step advancement depending on step orientation is shown in Figure 4. Advancing rates of the *r*-oriented steps (black arrow) are faster than those of the [101]-oriented steps (white arrow). Quantitative measurements of step velocity as a function of orientation are discussed below.

**4. Step Velocity versus Scanning Rate.** In AFM measurements, the tip approaches the crystal surface and scans at a high

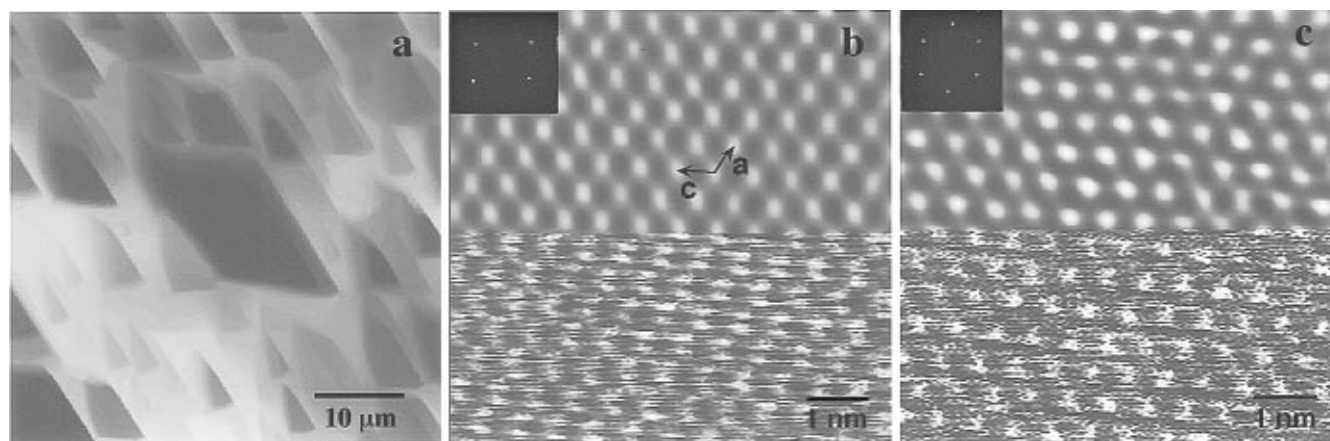


**Figure 2.** Macroscopic etch pit and atomic images of the DCPD (010) face. (a) A rhomboidal etch pit appeared after etching with 1 N HCl. (b) Atomic image obtained *in situ* during the dissolution process. Two periodicities corresponding to the *a* and *c* axes of DCPD can be clearly distinguished. From this image, the orientations of the etch pit in *a* are found to be [001] and [101]. (c) Pseudo-hexagonal atomic image.

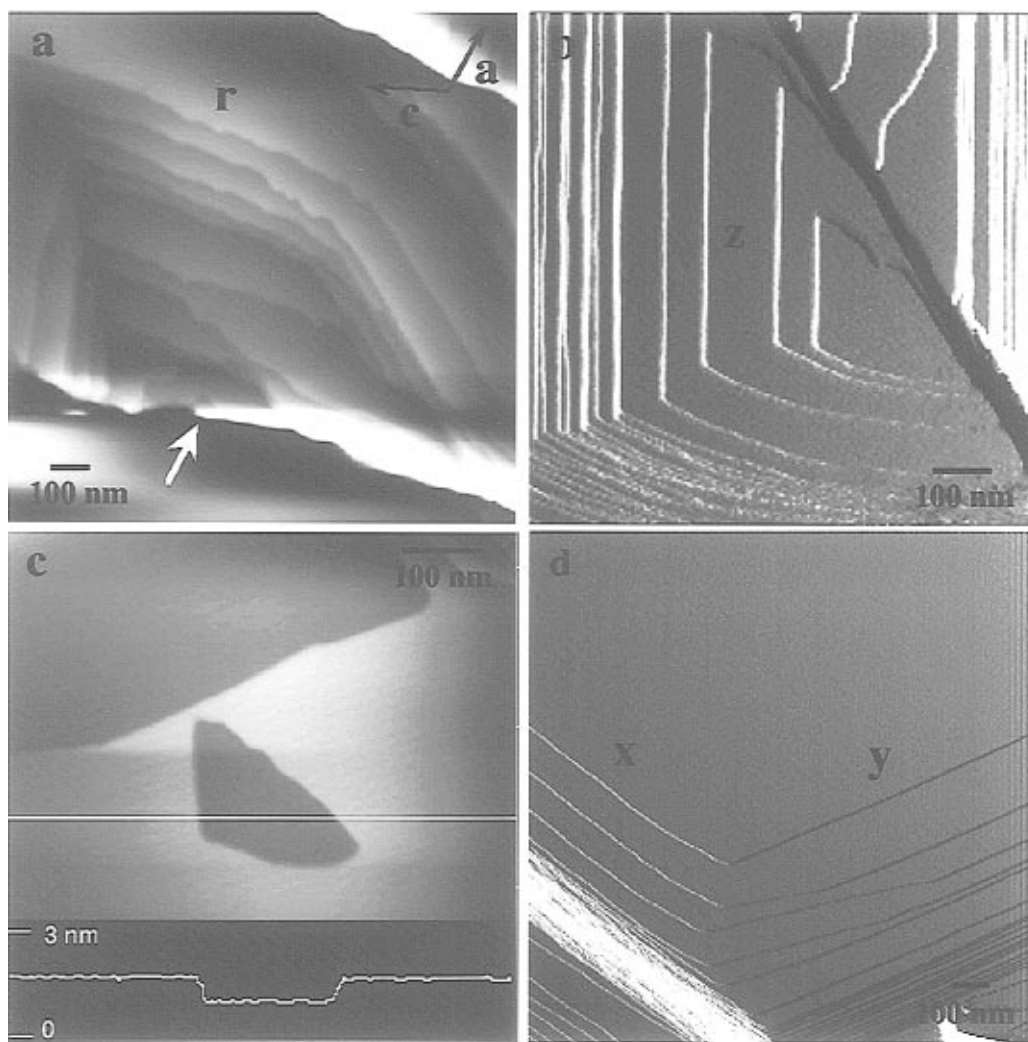


**Figure 3.** Three kinds of etch pits and steps observed during dissolution in the physiological solution. (a) Etch pit appears at a macrostep front. (b) Etch pit nucleating on a flat terrace with repeated formation of steps. (c) Isolated flat hole 0.75 nm deep surrounded by a closed step. (d) *x*- and *y*-oriented steps.

frequency. The diffusion boundary layer is agitated to some extent, which may affect dissolution kinetics. Thus, we measured the step velocities at different scanning rates to clarify the effect of scanning rates. Figure 5 shows the time and relative distance relationship for *y*-oriented steps at the scanning rates of 5 Hz (○) and 10 Hz (●). It is not possible to investigate step advancement in real time at scanning rates lower than 5 Hz. Measurements were performed for steps of the same origin. Data

lie on a straight line which indicates that each step advances at a constant velocity and fluctuation or instability of advancing rates is negligible. The velocities are calculated to be  $2.4 \pm 0.3$  nm/s for the 5 Hz scanning rate and  $2.6 \pm 0.2$  nm/s for the 10 Hz scanning rate. This result indicates that the step velocities are not affected by scanning rates, at least from 5 to 10 Hz. All measurements were thus performed within this range of scanning rates.

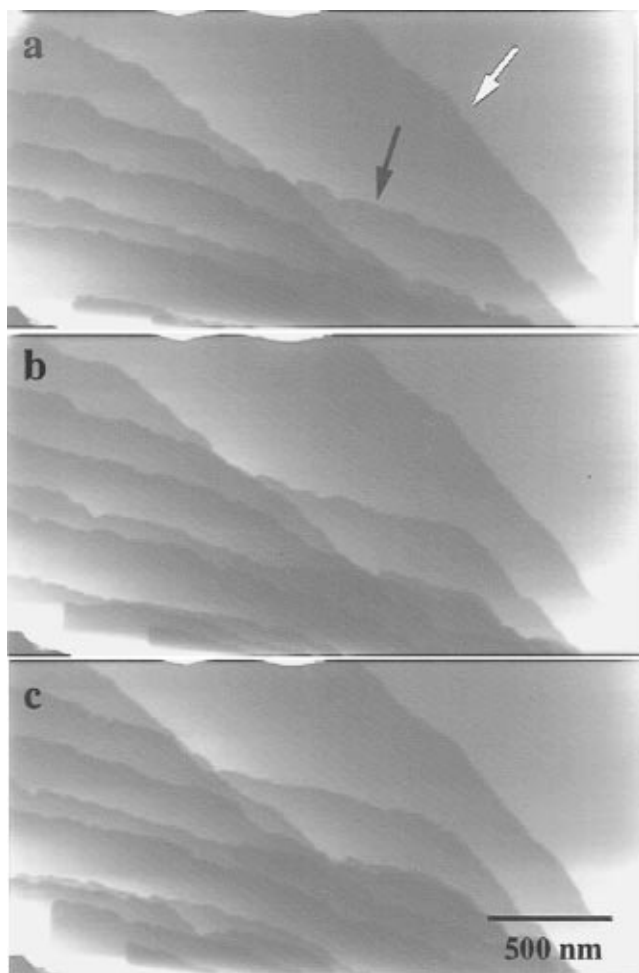


**Figure 4.** An example of anisotropic step advancement. *r*-oriented (black arrow) and [101]-oriented (white arrow) steps are shown. It can be seen that the *r*-oriented steps advance much faster than the [101]-oriented steps.

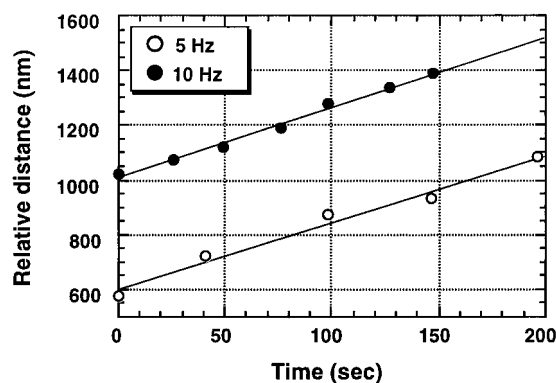


**Figure 5.** The relationship between time and relative distance for *y*-oriented steps, with scanning rate as a fixed parameter. Open and closed circles represent the results of 5 and 10 Hz scanning rates, respectively. No difference in the step velocities can be seen.

**5. Step Velocity versus Step Orientation.** Figure 6 shows the relationship between time and relative distance for *x* (●), *r* (○), *z* (▲), and [101] (□)-oriented steps. Although only the result of 1 step for each orientation is presented, more than 10 steps from the same origin were measured to determine average step velocities. A linear relationship between time and relative distance is observed for all orientations, and from the slope of each line, step velocities are calculated as  $0.31 \pm 0.04$  nm/s for *x*,  $1.6 \pm 0.4$  nm/s for *r*,  $1.5 \pm 0.1$  nm/s for *z*, and  $0.19 \pm 0.02$  nm/s for [101]. Compared with the *y*-oriented step velocity in the previous section, the *x*-oriented step velocity is about 8

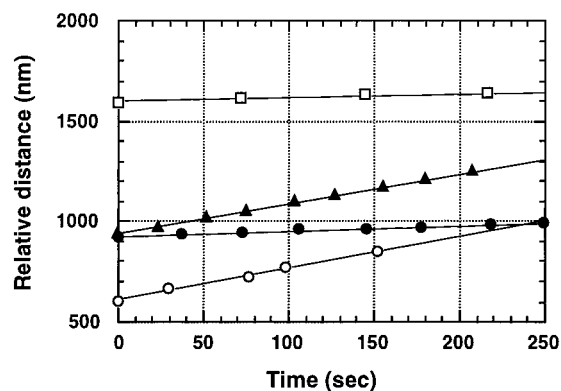


**Figure 6.** Time and relative distance relationship for *x* (●), *z* (▲), *r* (○), and [101] (□) steps. All steps show a linear relationship and the average velocity can be calculated from the slope of each line. The step velocity strongly depends on the orientation.

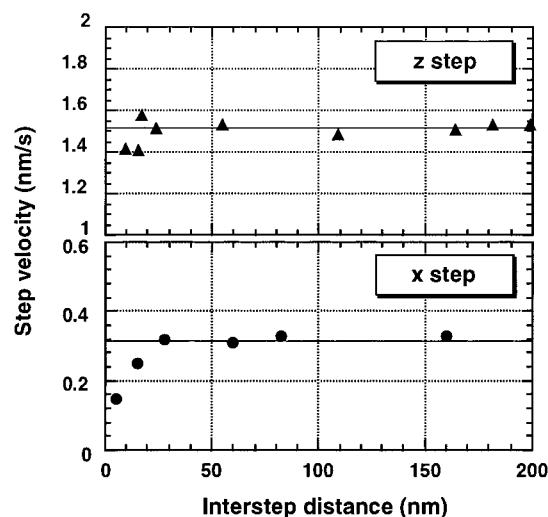


**Figure 7.** Relationship between step velocity and interstep distance. *x* (●)- and *z* (▲)-oriented steps were measured. For *z*-oriented steps, the critical interstep distance below which the step velocity starts to decrease is not clear, but for *x*-oriented steps, the step velocity obviously decreases when the interstep distance becomes smaller than 15 nm.

times smaller. Moreover, the difference in step velocities between *r*- and [101]-oriented steps is about one order of magnitude. From these measurements, step velocities are summarized as  $v_y > v_r \approx v_z \gg v_x > v_{[101]}$ . The error values for each step rate are 10–15%; however, that for the *r*-oriented step is relatively large, about 25%, due to the fact that the morphology of step fronts running parallel to this direction is unstable and shows irregular shape. On the other hand, *z*-oriented steps show regular morphology although their velocities are comparable to that of the *r*-oriented steps.

**6. Step Velocity versus Interstep Distance.** Interstep distance controls the step movement under the condition that the diffusion field developing around each step overlaps and step–step interaction occurs. In Figure 7, the relationship between step velocity and interstep distance is shown. Measurements were performed both for *z* (▲)- and *x* (●)-oriented steps. For the *z*-oriented steps, although a clear relationship is not seen, the step velocities seem to slightly decrease as the interstep distance decreases from 15 to 10 nm. The *x*-oriented step velocities are clearly observed to decrease when the interstep distance decreases from 15 to about 5 nm. The step velocity at an interstep distance of 5 nm is almost half that at an interstep distance of  $>30$  nm. The critical interstep distance below which the step velocity starts to decrease is thus estimated to be about 15 nm.

## Discussion

In the present study, the following findings were made. 1. Dissolution proceeds via nucleation of etch pits and step flow from the crystal edge. Spiral dissolution steps were rarely observed. 2. Step velocity strongly depends on the orientation of steps. 3. Step velocity is not affected by scanning rate. 4. Step–step interaction occurs when the interstep distance decreases to about 15 nm.

From the viewpoint of the rate-determining process, it can be said that volume diffusion has no effect on the overall dissolution rate of the DCPD under the present conditions. If volume diffusion was the rate-determining process, anisotropic step velocity, which is dependent on step orientation, would not be expected. Equal step velocities at different scanning rates supports this conclusion. These results indicate that the rate-determining process for DCPD dissolution is the surface process. From the results of step–step interaction and critical interstep distances, it is clear that the surface process involves both detachment of molecules at the step front and surface diffusion. Both can result in anisotropic step velocity depending on the orientation. The former contributes by providing anisotropic bond energies and the latter, the differences in jump distances of molecules for diffusion to each step. We estimate the contribution of each process by calculating the ratio of step kinetic coefficient  $\beta_{st}$  to the characteristic diffusion rate  $D_s/\lambda_s$ .  $\lambda_s$  and  $D_s$  are surface diffusion length and surface diffusion coefficient, respectively. When  $\beta_{st}\lambda_s/D_s \gg 1$ , the process is controlled by surface diffusion; when  $\beta_{st}\lambda_s/D_s \ll 1$ , detachment of molecules at the step front becomes the major resistance to the dissolution.<sup>21</sup> From step velocity measurements,  $\beta_{st}$  and  $\lambda_s$  are directly defined. When the impurity effect for the step advancement can be neglected as in the present case, which was confirmed by atomic image of the dissolved surface, the step velocity without step–step interaction can be simply expressed as  $v = \beta_{st}\omega C_e\sigma$ , where  $\omega$ ,  $C_e$ , and  $\sigma$  are specific molecular volume, equilibrium concentration, and relative undersaturation, respectively. Taking into account the elementary step height, which is half of the lattice parameter of the  $b$  axis, i.e., 0.75 nm, and crystal symmetry,  $\omega$  is calculated as  $6.18 \times 10^{-29} \text{ m}^3$ .  $\sigma$  is defined as,  $\sigma = 1 - C/C_e$ , where  $C$  and  $C_e$  are actual solution concentration and saturated concentration, respectively. At the same pH value,  $C/C_e$  is approximately the ratio of the mean ionic activity in the solution to the saturated solution. The mean ionic activity can be expressed by use of ioninc activity product  $I_p$  as  $I_p^{1/n}$ .  $n = 2$  represents the number of ions in a formula of DCPD. When the solution is saturated,  $I_p$  corresponds to the solubility product of DCPD,  $K_{sp}$ . Thus, the  $\sigma$  can be expressed by using  $I_p$  and  $K_{sp}$  as  $\sigma = 1 - (I_p/K_{sp})^{1/2}$ .  $K_{sp}$  is  $2.57 \times 10^{-7}$  at 25 °C from ref 12 and  $I_p$  was calculated as  $10^{-6.70}$  using the program of Maekawa.<sup>24</sup> Relative undersaturation  $\sigma$  is thus 0.12 for the present solution. Using these parameters, the values of  $\beta_{st}$  are  $4.6 \times 10^{-4}$ ,  $3.0 \times 10^{-4}$ ,  $0.56 \times 10^{-4}$ , and  $0.35 \times 10^{-4} \text{ m/s}$ , for  $y$ -,  $r(z)$ -,  $x$ -, and  $[101]$ -oriented steps, respectively. On the other hand,  $\lambda_s$  is estimated to be 7.5 nm from the relationship between step velocity and interstep distance. This value is 5–6 times smaller than that estimated in previous studies.<sup>22</sup>  $D_s$  is calculated using following relations:

$$K_{ad} = \exp[(E_d - E_a)/kT] \quad (1)$$

$$\lambda_s = a \exp[(E_d - E_s)/2kT] \quad (2)$$

$$D_s = a^2(kT/h)\exp(-E_s/kT) \quad (3)$$

In these equations, the adsorption coefficient  $K_{ad}$  and the activation energy for adsorption  $E_a$  cannot be calculated directly

from our study, thus we use reported values,  $K_{ad} = 120$  and  $E_a = 42 \text{ kJ/mol}$ , by Zhang and Nancollas.<sup>22</sup> Using these values,  $E_d$  is calculated as 54 kJ/mol from eq 1.  $E_s$  is thus 39 kJ/mol from eq 2 assuming the size of growth unit  $a$  is 0.39 nm. The surface diffusion coefficient  $D_s$  at 25 °C is therefore  $1.18 \times 10^{-13} \text{ m}^2/\text{s}$  from eq 3. As the  $\lambda_s$  is 7.5 nm, the characteristic surface diffusion rate  $D_s/\lambda_s$  is  $1.6 \times 10^{-5} \text{ m/s}$ . Using the calculated  $\beta_{st}$ ,  $0.35\text{--}4.6 \times 10^{-4} \text{ m/s}$ , for each oriented step, the ratio  $\beta_{st}\lambda_s/D_s$  is 2.2–29. Compared with the case of  $\text{KH}_2\text{PO}_4$ ,  $\text{NH}_4\text{H}_2\text{PO}_4$   $\{101\}$  faces, which were thought to exhibit surface diffusion limited growth,<sup>25–27</sup> the present ratio is more than two orders of magnitude smaller but two to three orders of magnitude larger than the case of a hydroxyapatite  $\{10\bar{1}0\}$  face, in which the incorporation of molecules at the step front completely controls the growth process,<sup>5</sup> if we assume that surface diffusion coefficients are the order of  $10^{-13} \text{ m}^2/\text{s}$  for each crystal which is thought to be ordinary value in the solution growth judging from the study for KDP and ADP by Chernov<sup>21</sup> and his co-workers. We estimate the contribution of surface diffusion and detachment kinetics by calculating activation energies. The activation energy for step advancement is directly determined using  $\beta_{st}$ , i.e.,  $\beta_{st} = a\zeta(kT/h)\exp(-E/kT)$ , where  $E$  is the activation energy for step advancement and  $\zeta$  is the kink density per unit atomic site on the step. Assuming that  $\zeta = 0.1\text{--}1$ ,  $E = 36\text{--}46 \text{ kJ/mol}$ .  $E$  involves  $E_a$ ,  $E_s$ , and the activation energy for detachment of molecules at step front  $E_{det}$ . The relation between them can be expressed;  $E \cong E_a - E_s + E_{det}$ .<sup>26</sup> From this relation,  $E_{det}$  is 33–43 kJ/mol. These values are almost the same as the activation energy for surface diffusion, 39 kJ/mol. This means that the dissolution process for DCPD under the present conditions is controlled both by detachment of molecules at the step front and a subsequent surface diffusion process, although the measured surface diffusion length was about 5–6 times smaller than the estimated value. The contribution of both processes is comparable and this result supports the conclusion of Zhang and Nancollas<sup>21</sup> who considered the importance of surface diffusion at low undersaturations.

## Conclusion

Dissolution kinetics of DCPD in pseudo-physiological solution was investigated by *in situ* AFM. It was found that the step velocity showed strong anisotropy depending on the orientation. The dissolution process was controlled by the detachment of molecules at the step front and subsequent surface diffusion. The contributions of the two processes are comparable.

## References and Notes

- (1) Gratz, A. J.; Hillner, P. E.; Hansma, P. K. *Geochem. Cosmochim. Acta* **1992**, *57*, 491.
- (2) Manne, S.; Cleveland, J. P.; Stucky, G. D.; Hansma, P. K. *J. Cryst. Growth* **1993**, *130*, 333.
- (3) Land, T. A.; Malkin, A. J.; Kuznetsov, Yu. G.; McPherson, A.; DeYoreo, J. J. *Phys. Rev. Lett.* **1995**, *75*, 2774.
- (4) Malkin, A. J.; Land, T. A.; Kuznetsov, Yu. G.; McPherson, A.; DeYoreo, J. J. *Phys. Rev. Lett.* **1995**, *75*, 2778.
- (5) Onuma, K.; Ito, A.; Tateishi, T.; Kameyama, T. *J. Cryst. Growth* **1995**, *154*, 118.
- (6) Glimcher, M. J.; Bonar, L. C.; Grynpas, M. D.; Landis, W. J.; Roufosse, A. H. *J. Cryst. Growth* **1981**, *53*, 100.
- (7) Rodgers, A. L.; Spector, M. *Calcif. Tissue Int.* **1986**, *39*, 342.
- (8) Brown, W. E.; Chow, L. C. *J. Dent. Res.* **1983**, *62*, 672.
- (9) Neuman, W. F.; Neuman, M. W. *Chemical Dynamics of Bone Mineral*; University of Chicago Press, Chicago, 1958.
- (10) Eanes, E. D.; Posner, A. S. *Trans. N. Y. Acad. Sci.* **1965**, *28*, 233.
- (11) Francis, M. D.; Webb, N. C.; *Calcif. Tissue Res.* **1971**, *6*, 335.
- (12) Doi, Y.; Eanes, E. D. *Jpn. J. Oral Biol.* **1987**, *29*, 25.
- (13) Royer, P.; Amrah-Bouali, S.; Freche, M.; Rey, C.; Rouquet, N.; Bonel, G. *Bioceramics* **1993**, *5*, 95.
- (14) Nancollas, G. H.; Marshall, R. W. *J. Dental Res.* **1971**, *50*, 1268.

- (15) Christoffersen, J.; Christoffersen, M. R. *J. Cryst. Growth* **1988**, 87, 41.
- (16) Christoffersen, M. R.; Christoffersen, J. *J. Cryst. Growth* **1988**, 87, 51.
- (17) Zhang, J.; Nancollas, G. H. *J. Dental Res.* **1987**, 66, 219.
- (18) Gilmer, G. H.; Ghez, R.; Cabrera, N. *J. Cryst. Growth* **1971**, 8, 79.
- (19) Garside, J.; Janssen-van Rosmalen, R.; Bennema, P. *J. Cryst. Growth* **1975**, 29, 353.
- (20) Van der Eerden, J. P. *J. Cryst. Growth* **1982**, 56, 174.
- (21) Chernov, A. A. In *Modern Crystallography III: Crystal Growth*; Vainshtein, B. K., Chernov, A. A., Shuvalov, C. A., Eds.; Springer: Berlin, 1984.
- (22) Zhang, J.; Nancollas, G. H. *J. Cryst. Growth* **1992**, 125, 251.
- (23) Curry, N. A.; Jones, D. W. *J. Chem. Soc. A* **1971**, 3725.
- (24) Maekawa, K. M.S. Thesis. Waseda University, Tokyo, Japan, 1995.
- (25) Vekilov, P. G.; Kuznetsov, Yu. G.; Chernov, A. A. *J. Cryst. Growth* **1992**, 121, 44.
- (26) Vekilov, P. G.; Kuznetsov, Yu. G.; Chernov, A. A. *J. Cryst. Growth* **1992**, 121, 643.
- (27) De Yoreo, J. J.; Land, T. A.; Dair, B. *Phys. Rev. Lett.* **1994**, 73, 838.